

pubs.acs.org/journal/apchd5 Article

Giant Gate-Tunability of Complex Refractive Index in Semiconducting Carbon Nanotubes

Baokun Song, Fang Liu, Haonan Wang, Jinshui Miao, Yueli Chen, Pawan Kumar, Huiqin Zhang, Xiwen Liu, Honggang Gu, Eric A. Stach, Xuelei Liang, Shiyuan Liu,* Zahra Fakhraai, and Deep Jariwala*



Cite This: https://dx.doi.org/10.1021/acsphotonics.0c01220



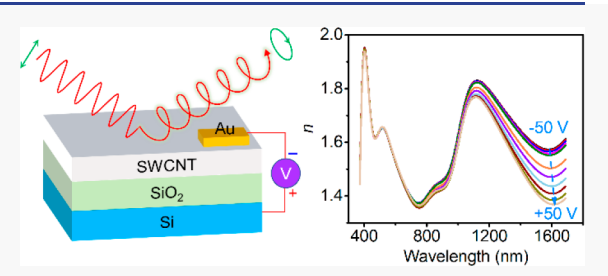
ACCESS

III Metrics & More

Article Recommendations

Supporting Information

ABSTRACT: Electrically tunable optical properties in materials are desirable for many applications ranging from displays to lasing and optical communication. In most two-dimensional thin films and other quantum-confined materials, these constants have been measured accurately. However, the optical constants of single-walled carbon nanotubes (SWCNTs) as a function of electrostatic tuning are yet to be measured due to a lack of electronic purity and spatial homogeneity over large areas. Here, we measure the basic optical constants of ultrathin high-purity (>99%) semiconducting single wall carbon nanotube (s-SWCNT) films



with spectroscopic ellipsometry. We extract the gate-tunable complex refractive index of s-SWCNT films and observe a giant modulation of the real refractive index (\sim 11.2% or an absolute value of >0.2) and extinction coefficient (\sim 11.6%) in the near-infrared (IR) region (1.3–1.55 μ m) induced by the applied electric field significantly higher than all existing electro-optic semiconductors in this wavelength range. We further design a multilayer IR reflection phase modulator stack by combining s-SWCNT and monolayer MoS₂ heterostructures that can attain >45° reflection phase modulation at 1600 nm wavelength for <200 nm total stack thickness. Our results highlight s-SWCNTs as a promising material system for infrared photonics and electro-optics in telecommunication applications.

KEYWORDS: semiconducting carbon nanotube, gate-tunable complex refractive index, electro-optic effect, spectroscopic ellipsometry

The complete knowledge of optical constants of a material is essential for its applicability in the design and development of optoelectronic, photonic, and electro-optic (EO) devices. Over the years, the knowledge of optical constants to a high degree of accuracy has been an essential component of materials development and applications research in optoelectronics. The most basic and widely known optical constants of a material arise from its electronic dispersion and are called the complex refractive index: the real part is the refractive index given by Snell's law, and the imaginary part is the extinction coefficient. Dynamic tuning of these optical constants with external stimuli such as heat, light, strain, and magnetic or electric field is the basis of optical modulation. 1—3

The optical modulator is one of the most important components/devices in any optical interconnect link and lies at the heart of telecommunications and internet hardware. Its primary function is to modulate the attributed parameters (amplitude, phase, and polarization) of light in the time or frequency domain. Based on the above-discussed stimuli to modulate optical constants, optical modulators can be classified as all-optical, EO, magneto-optic, acousto-optic, and mechano-optical modulators and so on.^{2,3} Among them, EO modulators are the most promising due to the simplicity of applying voltages to microfabricated electrodes and ability to minimize parasitic circuit elements. The performance of EO modulators strongly

depends on the EO effect of component materials.⁴ This is especially important in the telecommunication region (1.3–1.5 μ m), which represents the loss minima in the spectrum of optical fibers. Therefore, new semiconductor materials that demonstrate a large EO effect in this wavelength range are highly desirable.

Silicon (Si), which is the semiconductor of choice, exhibits extremely weak inherent electric-refractive (ER) and electric-absorption (EA) at two important telecommunication wavelengths, 1.3 and 1.55 μ m. This can be traced back to the natural lack of Pockels effect and negligible Franz-Keldysh effect. Thus, most of the silicon photonics devices rely on the plasma dispersion effect (PDE) to tune optical constants, while these silicon modulators usually need extremely high extra carrier density to achieve appropriate optical modulation. To overcome these drawbacks of Si, Quantum Well (QW) structures of III–V semiconductors (GaAs, InP, and their alloys) have been developed that exhibit a stronger EO effect,

Received: August 2, 2020 Published: September 23, 2020



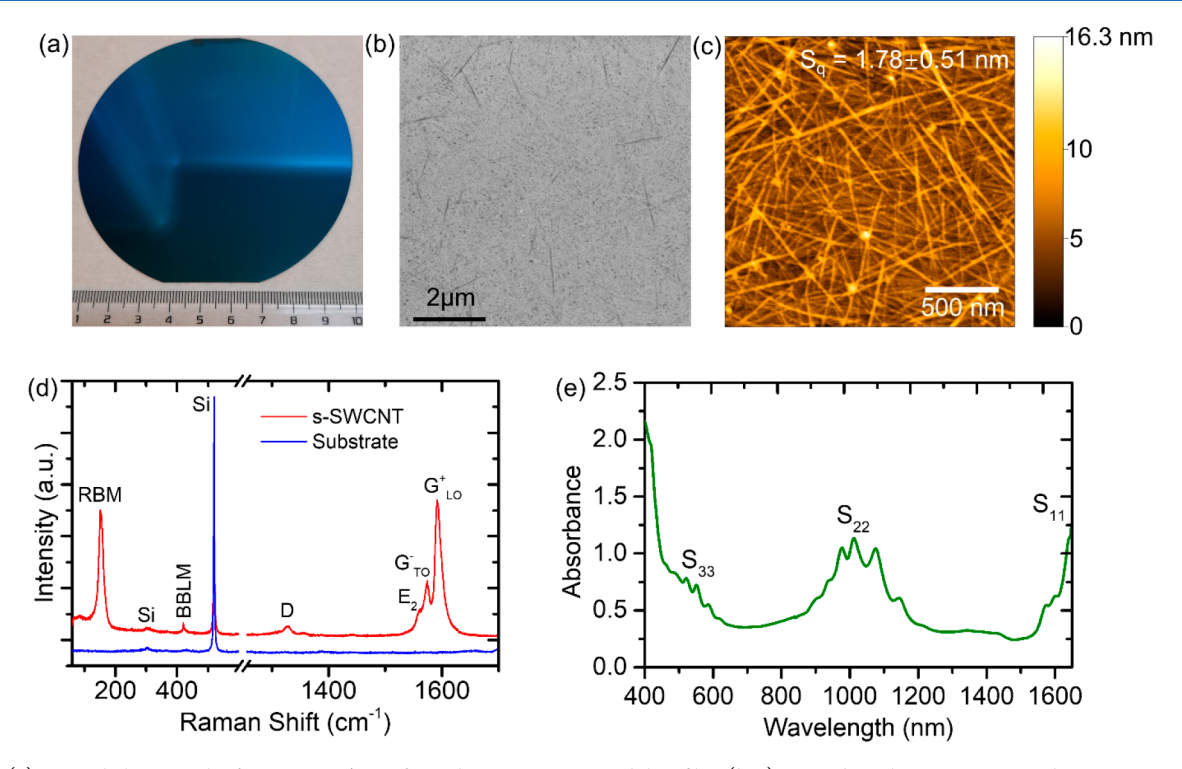


Figure 1. (a) Optical photograph of a 4 in. SiO_2/Si wafer with s-SWCNT coated thin-film. (b, c) Secondary electron scanning electron micrograph and topographic image acquired using atomic force microscopy of the s-SWCNT film, the scan area in (c) is $2 \mu m \times 2 \mu m$. (d) Typical Raman spectrum of the film on SiO_2 (324 nm)/Si wafer. (e) Absorbance spectrum of the s-SWCNT dispersion in chloroform.

namely, quantum-confined Stark effect (QCSE).8 Modulators based on QCSE can achieve narrow-band, high-efficiency EA; however, the complex fabrication requirements and CMOS compatibility still limit their widespread applications. The advent of atomically thin, van der Waals (vdW) materials, such as graphene, has created interesting possibilities for EO modulation, including integration on Si and harnessing hybridization with phonon polaritons of polar materials such as SiC^{10,11} and h-BN^{12,13} that have proven to be the superior substrates for graphene.^{3,14} While the intrinsic modulation depth of monolayer (1L) graphene-based devices can only be up to ~0.1 dB due to the small absorptance 2.3%.3 The use of waveguides or resonant optical cavities integrated with graphene can meet the performance requirements of short-range optical interconnects in Si-based integrated photonics. Beyond graphene, optical constants of two-dimensional (2D) transitional metal dichalcogenides (TMDCs; 2D-WS₂ and 2D-MoS₂) have also shown to exhibit giant tunability via application of a gate voltage due to the presence of strongly bound excitons. 15,16 However, due to the visible frequency band-gaps of these materials and their excitonic transitions, they are not suitable for the telecommunication applications.

In comparison, semiconducting single wall carbon nanotubes (s-SWCNT) are a well-studied yet extremely promising material platform that can be used to design infrared (IR) EO devices. Carbon nanotubes are structurally and electronically quantum-confined in one dimension and, therefore, possess intrinsically discrete absorption singularities, ¹⁷ large exciton binding energy, ¹⁸ and gate-tunable optical properties, ^{19,20} as well as good CMOS compatibility, ²¹ which are superior to their 2D counterparts in many respects. Electro-absorption properties of s-SWCNT have been studied previously, ^{21,22} however, to our best knowledge, a reliable and systematic study on the gate-tunable inherent optical constants of s-SWCNTs, such as

refractive index and extinction coefficient, has not yet been reported. This is mainly because of the lack of high electronic purity in the samples and the difficulty in controlling the film thickness and uniformity over a large area. The lack of electronic purity introduces high conductance and screening from the metallic nanotube impurities which prevents reliable gate modulation.²² However, over the past decade, several advances have been made in purification and deposition of s-SWCNT films that render this possible in our study.^{23–29}

In this paper, we determine the gate-tunability of the basic optical constants of ultrathin s-SWCNT films, including refractive index n, extinction coefficient κ , and absorption coefficient α . We find that the optical constants of s-SWCNT in near-IR region show striking changes and excellent sensitivity with the gate voltage (V_G) . The electric field-induced changes in n and κ (Δn , $\Delta \kappa$) of s-SWCNT is much greater than those of traditional semiconductors, such as Si, Ge, and GaAs. The remarkable Δn , $\Delta \kappa$, excellent Si-CMOS compatibility, $^{27,30-32}$ and low fabrication complexity renders s-SWCNTs as attractive candidates for designing IR photonic devices specially in the telecommunications band. Beyond determining and comparing field and density tunable optical constants, we show an ultrathin IR gate-tunable reflection phase modulator stack with a superlattice structure of (1L-MoS₂/s-SWCNT)₅/MoS₂/Au, which shows theoretical phase change exceeding 45° ($\pi/4$) for ~100 nm active layer s-SWCNT phase modulator in the stack for $\lambda = \sim 1600$ nm. This phase-tuning was achieved without the need for any nanostructuring or nanopatterning into a metasurface, which is noteworthy. The gate-tunable optical constants of s-SWCNTs reported here could provide theoretical guidance for next-generation Si CMOS-compatible photonics and optoelectronics devices, as well as IR photodetectors, sensors, modulators, and energy harvesters.

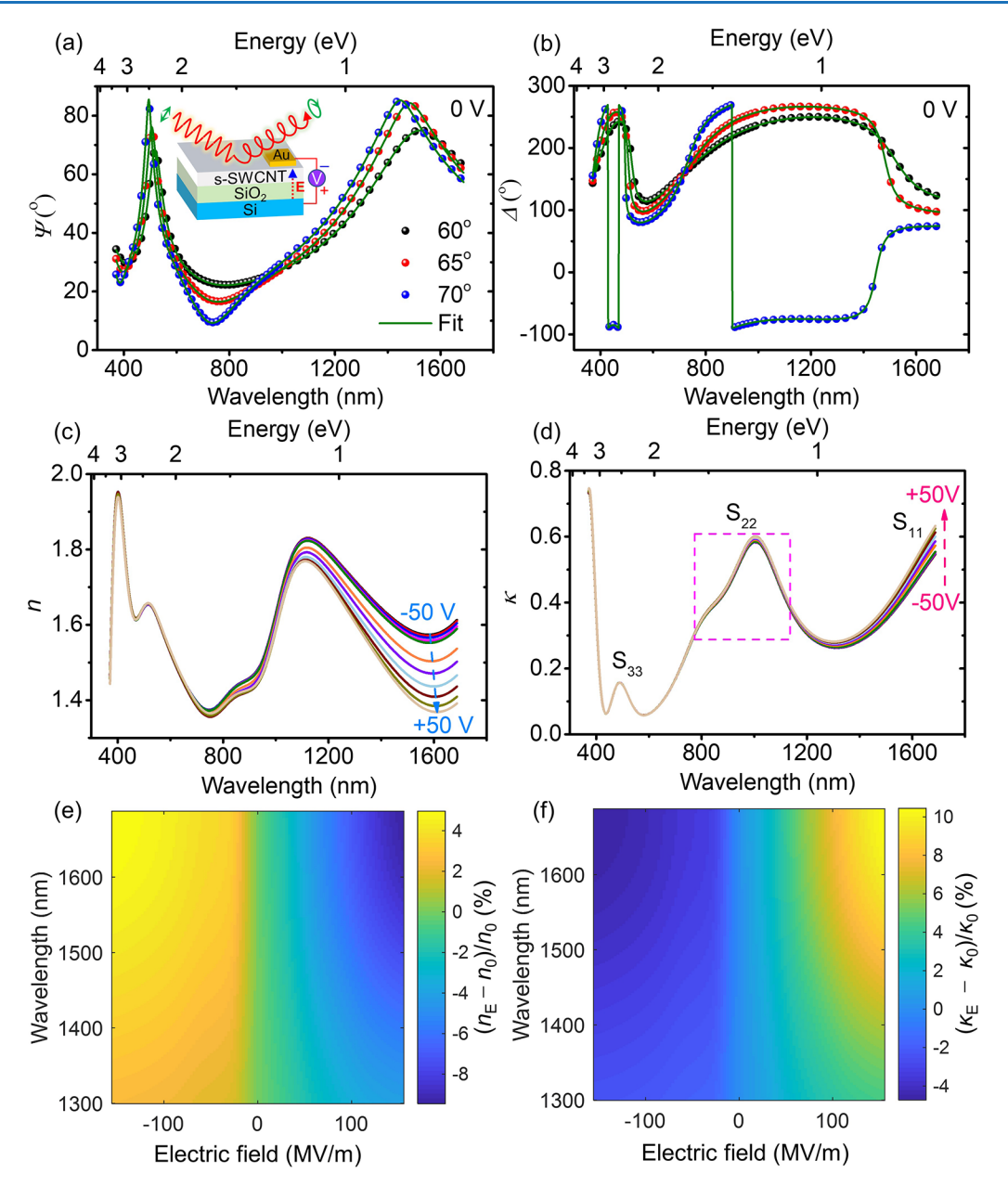


Figure 2. (a, b) Measured (spheres) and best-fits (lines) of multiangle incident (60°, 65°, and 70°, w.r.t. normal incidence) ellipsometric spectra of s-SWCNT film. For clarity, only fitting results for zero applied volts are plotted. The inset in (a) shows the schematic of SE measurement that is used to measure the s-SWCNT specimen under applied gate voltage. (c) Gate-tunable n of s-SWCNT, the voltage changes from -50 V to +50 V with a step size of 10 V. The large modulation in n between 1100 and 1687 nm is apparent from the plots. (d) Gate-tunable κ on the same voltage and spectral range with relatively small modulation between 1200 and 1687 nm. The pink dash square in (d) indicates the shoulder and peak region that is attributed to the S_{22} transition. (e, f) Relative changes of n and κ with the applied electric field over the near-IR region (1300–1687 nm). n_E (κ_E) and n_0 (κ_0) stand for the refractive indices (extinction coefficients) in the presence and absence of an applied electric field, respectively.

RESULTS AND DISCUSSION

We deposit ultrathin films of s-SWCNT directly on a 4 in. SiO₂/Si by dip-coating using a chloroform-dispersed high-purity (>99%) semiconducting SWCNT dispersion (prepared by Arc discharge method).^{23,24} The optical photograph and scanning electron microscopy (SEM) image of the s-SWCNT film specimen are shown in Figure 1a,b, where the uniform optical contrast and flat surface morphology suggest that the film is macroscopically and microscopically uniform. The dark lines that appear on the film surface in SEM micrograph (Figure 1b) are attributed to a small number of bundles. Figure 1c shows a representative atomic force microscopy (AFM) topography

image of the film which indicates a random structure of the network and root-mean-square surface roughness (S_q) of the film is estimated to be $\sim 1.78 \pm 0.51$ nm. These roughness values are much smaller than the spot size of our measurements (~ 2 mm) and wavelength of light (371-1687 nm). The taller and wider tube-like features in the AFM image can be interpreted as overlapping two or more tubes and bundles (thick white lines and nodes in Figure 1c). The nominal diameters of the suspended s-SWCNTs in the solution are about 1.4–1.6 nm, and the average length is $\sim 1.5-2~\mu m$ based on an earlier published report. We have further characterized the s-SWCNT films using Raman spectroscopy, which is sensitive to electronic character and chirality. A representative Raman

spectrum of the SWCNT film is shown in Figure 1d. Six typical Raman modes/features can be identified: radial breathing mode (RBM) at ~ 153 cm⁻¹, bundle breathing-like mode (BBLM) at \sim 420 cm⁻¹,³² D-band at \sim 1328 cm⁻¹, weak E₂ feature at \sim 1561 cm⁻¹ associated with the symmetry phonons,^{33,34} G⁺ feature at ~1591 cm⁻¹ resulting from the in-plane vibrations along the tube axis (longitudinal optical (LO) phonon mode), and a diameter-dependent G⁻ feature at ~1574 cm⁻¹ for in-plane vibrations along the circumferential direction (transverse optical (TO) phonon mode).³³ The G-band with clear Lorentzian lineshape (Figure S1(f)) indicates that our SWCNT film is comprised of only semiconducting tubes.³³ The appearance of weak Si mode at 303 cm⁻¹ suggests that the Raman responses were predominantly from the s-SWCNTs.³³ Additional Raman analysis suggests that the film is predominantly comprised of two types of nanotubes of diameters d_{t1} and d_{t2} at about 1.62 and 1.55 nm corresponding to (17,6) and (16,6) chirality, respectively. Both of these chiral indices belong to semiconducting tubes in the families of 40 and 38.35 Additional analysis and calculations are provided in Supporting Information, Figures S1 and S2. Finally, we also measure the absorbance spectrum of the nanotube solution in chloroform used for the deposition of the film (Figure 1e). The absorbance spectrum shows three prominent semiconducting absorption bands (S_{22} , S_{33} , and the rising side to the right of the S_{11}), as labeled in Figure 1e. 25,36,37 There is no obvious or discernible metallic transition peaks M_{11} (~615 nm) in the absorbance spectrum, ³⁶ further suggesting that the SWCNT film is mainly comprised of semiconductor tubes. Further information about the sample fabrication process and quality characterization can be found in ref 23 and in the Supporting Information.

Upon structural and basic optical characterization of the s-SWCNT films, we determine the gate-tunable complex refractive index via spectroscopic ellipsometry (SE) (Figure 2). The inset in Figure 2(a) illustrates the measurement configuration/schematic of the experiment, where a gold electrode (L \times W \times H: 0.5 mm \times 0.5 mm \times 50 nm) is deposited onto the surface of s-SWCNT film via thermal evaporation through a stencil shadow mask. The ellipsometry spot is positioned away from this gold electrode to completely lie in the s-SWCNT film region while the Au electrode is bonded. The degenerately *n*-type doped Si underneath the 324 nm thick SiO_2 is used as the back gate. When V_G changes from -50 V to 0 (0 to +50 V), extra holes (electrons) will be injected into the s-SWCNT film which modulate the optical properties. Subtle changes in the interaction between light and s-SWCNT film induced by carrier injection can be collected by the ellipsometer and recorded in a set of multiangle ellipsometric spectra $[\Psi(\lambda)]$, $\Delta(\lambda)$] (solid balls in Figure 2a,b). The measured ellipsometric spectra are fitted using theoretical plots (lines in Figure 2a,b) calculated from the transfer matrix method (TMM).³⁸ The fitting goodness is evaluated by the root-mean-square error (RMSE). It is calculated $\frac{1}{2p-q} \sum_{i}^{p} [(\Psi_{\text{exp}}^{i} - \Psi_{\text{cal}}^{i})^{2} + (\Delta_{\text{exp}}^{i} - \Delta_{\text{cal}}^{i})^{2}] \times 1000,$

where p and q refer to the number of wavelengths and the number of fitting parameters, and the subscripts "exp" and "cal" denote the experimental and calculated data. Regardless of whether the s-SWCNT film is in a finite bias or floating or grounded state, the value of RMSE in the ellipsometric analysis is as low as \sim 4.83, meaning that the analysis is reliable. For clarity, we only show the fitting results of s-SWCNT for electrically floating (unbiased) films ($V_{\rm G}=0$). The ellipsometric

spectra and related analysis results of s-SWCNT under different $V_{\rm G}$ can be found in Figures S4 and S5 of the Supporting Information. The thicknesses of s-SWCNT and SiO $_2$ determined by SE are 2.04 and 324 nm, which is consistent with the extracted results from the Raman spectrum. Additional principles, measurement process details, and data analyses about SE measurement are available in the Supporting Information and previous publications.

Figure 2c,d demonstrates the gate-dependent complex refractive index of s-SWCNT films. The three semiconducting absorption peaks (S₁₁-S₃₃) can be observed again in the extinction coefficient spectrum, and the wavelength positions of S₁₁-S₃₃ are consistent with the results of the absorbance spectrum of the dispersion in chloroform (Figure 1e). When $V_{\rm G}$ changes from -50 V to +50 V, n shows a significant decrease; on the contrary, κ exhibits a slight increase in the near-IR spectral region. This observation is in agreement with the evolution rules of Ψ and Δ spectra, as shown in Figure S4(c,d). The Δ spectrum is more sensitive to $V_{\rm G}$ than the Ψ spectrum ($\delta\Delta$ = 3° and $\delta\Psi$ = 0.6° when $V_{\rm G}$ changes from -50 V to +50 V), which leads to the significant change of n. The gating tunability of n and κ can be interpreted by PDE. Semiconducting SWCNTs are nominally p-doped in ambient conditions, which means they have an excess of holes. 44 The positive (negative) $V_{\rm G}$ decreases (increases) the hole concentration in the s-SWCNT film. Therefore, at high positive V_G , the s-SWCNT film is nearly intrinsic, with minimal excess free carriers. This minimizes the Pauli blocking⁴⁵ and enhances the oscillator strength of S_{11} , increasing the κ .²¹ Conversely, a negative V_G heavily p-dopes the sample and reduces the strength of the S_{11} transition. ^{21,22} We apply the above relationship to explain the V_G -modulated intensity change of κ (Figure 2d). When $V_{\rm G}$ changes from $-50~{\rm V}$ to +50 V, the density of holes will gradually reduce to intrinsic levels. This also corroborates with p-type character of thin-film transistors made from similar samples by the authors in the past. 23,24 Thus, κ increases monotonously as $V_{\rm G}$ changes from -50 V to +50 V. Prior studies have also observed similar changes in the absorbance spectra of CNTs. ^{21,22} The refractive index *n* of s-SWCNT gradually decreases with the increasing $V_{\rm G}$. This is in agreement with the relation between the injected carrier concentration and the change in $n(\Delta n)$, confirming that the evolution trend of *n* can also be well explained by PDE. A slight gate-dependent redshift appears in the IR portion of *n* spectra at \sim 1600 nm (close to S_{11} transition), as indicated by a blue arrow in Figure 2c. We infer that this shift is associated with the Stark effect in s-SWCNT, which can trigger some additional absorption below S₁₁ and S₂₂ transitions.

Here, it is worth mentioning that that complex refractive index of s-SWCNTs depends on the diameter of the nanotubes, that is, ER and RA should be different for the s-SWCNT films with different diameters. In order to verify this, we also prepared a high-purity HiPCO grown s-SWCNTs film on SiO2/Si substrate, as shown in Figure S6, whose diameter is in the range of \sim 0.8–1.1 nm, with an average length of about 1.5 μ m. The complex refractive index of HiPCO s-SWCNT films is determined by SE and shown in Figure S6(b,c). As compared with the Arc discharge s-SWCNTs, the complex refractive indices, optical transition energies and optical bandgaps of HiPCO s-SWCNT films are larger, which is expected due to the stronger 1D quantum confinement effect and tighter diameter distribution in smaller diameter tubes. 46,47 In addition to the diameter, the optical constants may also vary with the length of the s-SWCNTs. A larger average length of the s-SWCNT could

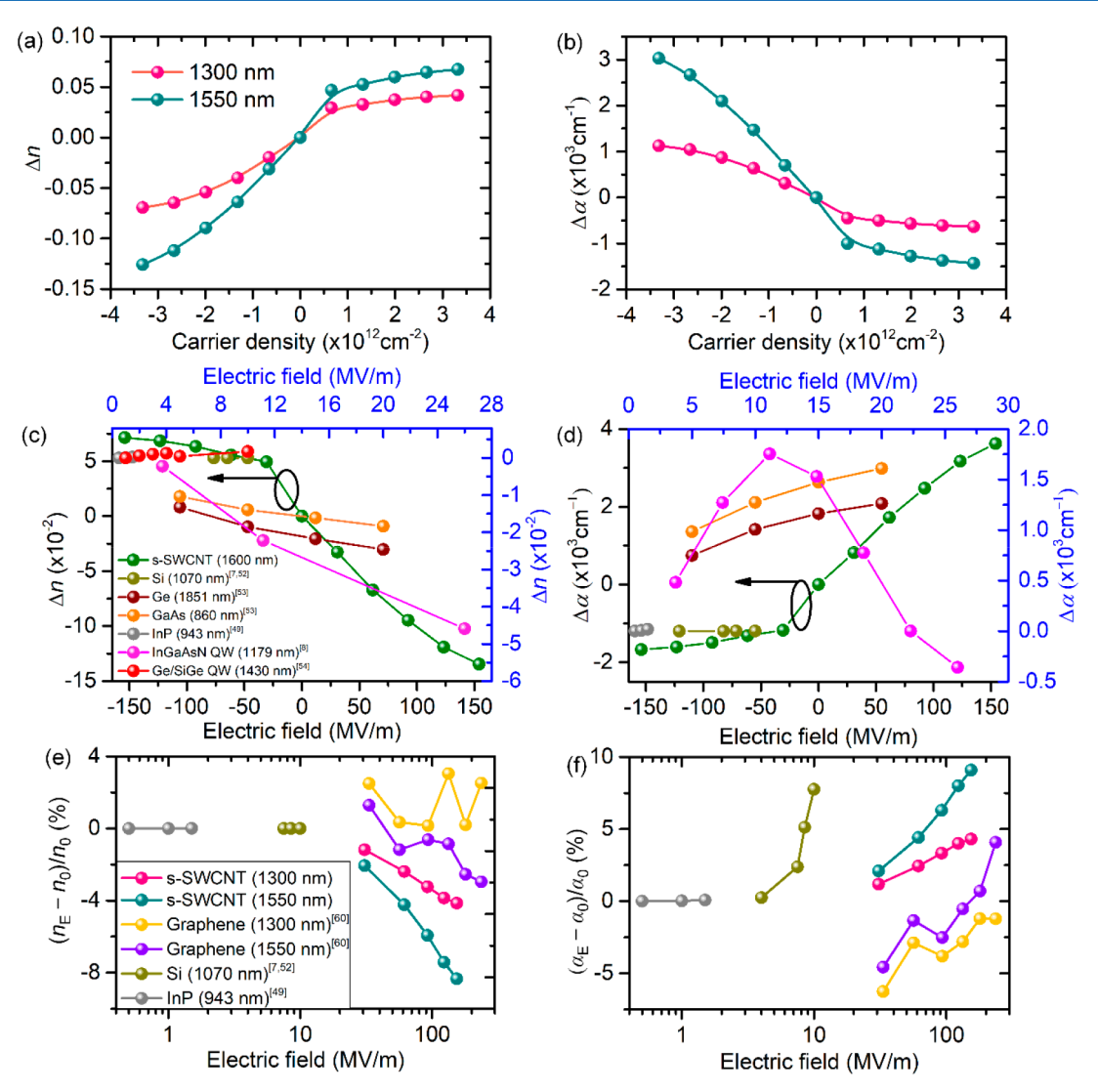


Figure 3. (a, b) Carrier concentration-dependent Δn and $\Delta \alpha$ of s-SWCNT at two critical telecommunication wavelengths 1.3 and 1.55 μ m, the positive "+" (negative "-") sign in the x-axes indicates the injection of holes (electrons) into the s-SWCNT film. (c, d) Δn and $\Delta \alpha$ of s-SWCNT films, some traditional semiconductor materials and QW structures used in EO modulators. Only the largest Δn and $\Delta \alpha$ reported by prior literatures are shown to make a fair comparison. Further, the Δn and $\Delta \alpha$ of s-SWCNT films are the largest at 1600 nm in the measured spectral region. The range of electric field over which the s-SWCNT films were measured is larger than other materials and, hence, plotted on the bottom x-axis and left y-axis for a fair comparison. The wavelengths in the figure legend indicate the spectral position from where the Δn and $\Delta \alpha$ are obtained. (e, f) Relative changes of n and α with the applied electric field of s-SWCNT, graphene, silicon, and InP, respectively. n_E (α_E) and n_0 (α_0) stand for the refractive indices (absorption coefficients) in the presence and the absence of an applied electric field, respectively.

increase the mean free path and mobility of the axially moving carriers, ultimately influencing the strength of the optical constants, such as optical conductivity and absorption.⁴⁸

Figure 2e,f displays the relative percentage changes of n and κ in the near-IR region with the external applied electric field estimated via parallel place capacitive coupling (see below). As compared with the extremely weak electric-field and carrier density induced changes of n and κ in traditional semiconductors, 1,49 the relative changes of n and κ in s-SWCNT can reach striking ~15% or an absolute value of >0.2. More importantly, the gate-tunability of n and κ is remarkably high at the two most useful telecommunication wavelengths, that is, 1.3 and 1.55 μ m.

Figure 3a,b illustrates the evolution of Δn and $\Delta \alpha$ (where $\alpha = 4\pi\kappa/\lambda$ is the absorption coefficient in cm⁻¹) of s-SWCNT at 1.3 and 1.55 μ m, with the carrier density N_c induced by V_G . N_c is calculated by N_c = $\varepsilon_0\varepsilon_{\rm SiO2}V_G/d_{\rm SiO2}$, where ε_0 and $\varepsilon_{\rm SiO_2}=3.9$

denote the free-space permittivity and static dielectric constant of ${\rm SiO}_2$, 50 and $d_{{\rm SiO}_2}=324$ nm. The trends of Δn and $\Delta \alpha$ as a function of $N_{\rm c}$ are opposite. The overall changes at 1.55 $\mu{\rm m}$ are greater (0.2 for Δn and 4500 cm⁻¹ for $\Delta \alpha$), as compared to those of 1300 nm, which can be mainly attributed to the greater influence from the enhanced ${\rm S}_{11}$ transition. Further, s-SWCNTs are also known to exhibit gate-tunable excitons and trions in the near-IR region, which may also influence this tunability. 51

Figure 3c,d shows comparative values of Δn and $\Delta \alpha$ for our sSWCNT films with some traditional semiconductors, including Si, ^{7,52} Ge, ⁵³ GaAs, ⁵³ and InP, ⁴⁹ as well as InGaAsN single QW and Ge/SiGe multiple QW structures, ⁵⁴ which have been studied or used for EO modulators. We choose to selectively display some of the largest Δn and $\Delta \alpha$ reported by prior literature to make a fair comparison. ^{7,8,49,52,52–54} It is obvious from the plots that Δn and $\Delta \alpha$ of s-SWCNTs are much more sensitive to the applied electric field than those of conventional

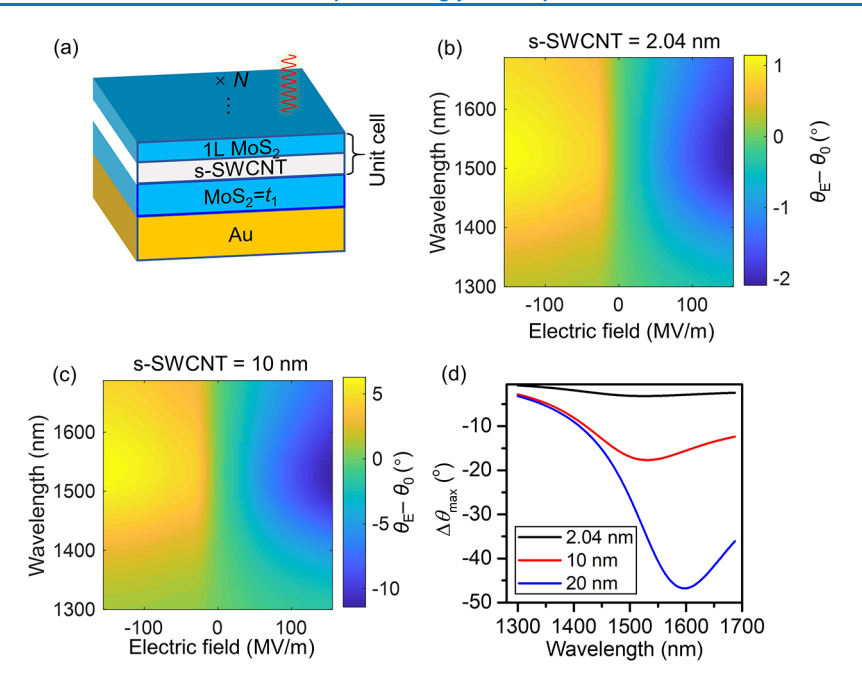


Figure 4. (a) Schematic of IR reflection phase modulator based on the s-SWCNT, MoS₂, and Au substrate. N and t_1 represent the number of unit cell and the thickness of bottom MoS₂ film. (b, c) Simulated gate-tunable reflection phase changes of structure (a) with 2.04 and 10 nm s-SWCNT, θ_E and θ_0 mean the reflection phases when the applied electric fields are E and 0. (d) Simulated maximum reflection phase differences as the applied electric field changes from -154 to +154 MV/m, where the thicknesses of s-SWCNT thin-films in the unit cell are 2.04, 10, and 20 nm, respectively. The N used in the simulation processes of (b)-(d) is 5.

semiconductors and EO material systems. With the increase of electric field, Δn and $\Delta \alpha$ of s-SWCNT, Ge, and GaAs decrease uniformly. Comparatively speaking, the magnitude of Δn and $\Delta \alpha$ of Si is very small ($\sim 10^{-6} - 10^{-5}$ and $\sim 0.05 - 5$ cm⁻¹), ⁷ which is associated with the inherent lack of Pockels effect, and the weak Franz-Keldysh effect.⁵ InP is another typical material platform for integrated photonics.⁵⁵ As shown in Figure 3c, the intensity of Δn of InP ($\sim 5 \times 10^{-5}$) is a little bit larger than that of Si. By exploiting the quantum confinement induced concentration of density of states, QCSE has also been used as the EO effect to design quaternary InGaAsN QWs based modulators, however, their compatibility with the Si CMOS is far from ideal. Likewise, Ge/SiGe QWs have also been used in EO modulators, 9,54 which help overcome the challenge of Si CMOS integration while exhibiting relatively high Δn $(\sim 10^{-4})^{54}$ and $\Delta \alpha$ ($\sim 2 \times 10^3$ cm⁻¹ when the applied voltage changes from 0 to 4 V). The tunability of the s-SWCNT refractive index is far superior even compared to ferroelectric electro-optic materials such as lithium niobite (LiNbO₃). LiNbO₃ is a classical material platform that has been widely adopted in phase modulators in telecommunications due to the highly efficient linear EO effect and good temperature stability. 56 Still, the index change (Δn_e) of LiNbO₃ can only reach ~0.02 (calculated by $\Delta n_e = -0.5 n_e^3 r_{33} E$; r_{33} means the element of electro-optic tensor and n_e is from ref 57) at 633 nm when a 100 MV/m electric field is applied along the crystal symmetry axis (z-axis). Likewise, photorefractive polymers with low glass transition temperatures also exhibit high refractive index modulation (~0.007 at 90 MV/m),⁵⁹ again, much lesser compared to s-SWCNTs. Recently, some studies have also observed ER and EA effects in semiconducting 2D TMDCs¹⁵ and black phosphorus (BP).⁴⁵ While the ER and EA effects in semiconducting 2D TMDCs are significant, the effects only appear at or around the excitonic transition peaks, which lie in the visible part of the spectrum. This limits the EO effect and its

applicability in the infrared region for semiconducting 2D TMDCs. Likewise, a strong and anisotropic EO effect has also been reported for ultrathin BP in our previous work. While the magnitude of the effect is large, the innate chemical instability of BP under ambient conditions combined with the lack of a large area, cm²-scale samples hinder its applicability to some extent, in addition to preventing the extraction of accurate optical constants.

In order to make a fair comparison on the same scale, we have normalized the Δn and $\Delta \alpha$ values over the positive electric field region to % change values in Figure 3e and f, respectively. The large % variation of s-SWCNTs in comparison to all others is evident. The large % change in α of silicon can be mainly attributed to the near-zero α_0 in the wavelength of 1070 nm. Furthermore, we also compare the Δn and $\Delta \alpha$ of s-SWCNT with those of monolayer graphene (Figure 3e,f).⁶⁰ It is found that the Δn of s-SWCNT thin-film with an applied electric field in the two telecommunication bands is comparable with that of the monolayer graphene, and with a clear monotonous trend, which is conducive to the design, development, and operation of the photonics devices. In summary, as compared to most of the traditional semiconductors and artificial QW structures, the mass production of s-SWCNT is relatively easy, and in recent years, the purification and deposition have also been perfected. Further, their Δn and $\Delta \alpha$ are far superior, especially in the telecommunication bands. Further, they possess good thermal stability, are fully compatible with Si CMOS-based heterointegration, and hence, are promising candidates for integratedphotonics and optoelectronics. ^{22,61} The specific values of Δn and $\Delta \alpha$ of these material systems shown in Figure 3c,d have been summarized in Table S2.

Finally, in order to intuitively illustrate the potential applications of the ultrathin s-SWCNT films and their unique optical constants, we propose and design an EO reflection phase modulator in the IR spectrum based on the s-SWCNT and MoS_2

as alternating layers in a superlattice structure (1L-MoS₂/s- $SWCNT)_N/MoS_2/Au$, where N refers to the number of the unitcell (1L-MoS₂/s-SWCNT). As shown in Figure 4a, bottom MoS₂ film, s-SWCNT film, and gold substrate are combined to form a structure analogous to a resonant Fabry-Perot cavity. In the near-IR region, the few-nm thick MoS₂ can be regarded as a lossless dielectric ($\kappa \approx 0$).⁶² MoS₂ is chosen for its vdW nature, high subgap index and literature precedent in combining it with s-SWCNT films in vdW heterostructure devices. 44 According to the electromagnetic wave interference theory, 63 a MoS₂ film with the minimum thickness of around $\lambda/4n_{\text{Mos}_2}$ (n_{Mos_2} is the refractive index of bulk MoS₂) together with the perfect reflector Au substrate will form a simple, lossless Fabry-Perot cavity in the near-IR part of the spectrum.⁶⁴ In this case, the normal incident light reflected by the Au/MoS2 interface will consequently produce a phase shift at the air/s-SWCNT interface after being modulated by the MoS2 film, thereby laying the foundation of designing a sensitive EO phase modulator⁶⁵ without the need for nanostructuring or creating a metasurface. We perform a simple parameter sweep in a thinfilm transfer matrix simulation and determine that when the thickness of bottom MoS₂ film (t_1) is \sim 72 nm, a maximum average reflection phase change -2.37° can be achieved in the s-SWCNT (2.04 nm) lying atop the MoS_2 . The average reflection phase change is defined as $\left[\sum_{i=1}^{M} (\theta_i^{+50V} - \theta_i^{-50V})\right]/M$, where $\theta_i^{+50~\mathrm{V}}$ and $\theta_i^{-50~\mathrm{V}}$ mean the reflection phases at the *i*th wavelength when the applied voltages are +50 V (+154 MV/m) and -50 V(-154 MV/m), M refers to the number of wavelengths (see Figure S7(a) in the Supporting Information). In this design, the overall maximum average phase change will increase proportionately when we increase N (see Figure S7(a-c) in the Supporting Information). Furthermore, the influence of the layer number (L) of MoS₂ in the unit-cell on the gate-tunable phase change is also considered in the simulation (Figure S7(d)). The optical constants and thickness (0.6 nm) of 1L-MoS₂ used here are taken from ref 41.

The performance of the superlattice stack IR reflection phase modulator can be further improved by increasing the thickness of s-SWCNT (Figure 4(b-d)). Here, we assume that the inplane complex refractive indices N_0 of s-SWCNT with different thicknesses are approximately equal to the isotropic complex refractive index shown in Figure 2c,d (detailed discussion can be found in Supporting Information). As illustrated in Figure 4c,d, when the thickness of s-SWCNT increases to 20 nm, the maximum reflection phase change of the multilayer stacking phase modulator can be over -45° . This $\pi/4$ phase shift in a simple multilayer stack without the need for creating a nanostructured metasurface is remarkable. Further, given that the total active layer s-SWCNT thickness is ~100 nm for our optimized stack of N=5, the above phase modulation at $\lambda=$ 1600 nm (\sim 16 \times the active medium thickness) is further noteworthy. Further, we have also designed an infrared absorber with maximum absorption approaching ~0.9 at 1550 nm based on the same structure (N = 5) shown in Figure 4a. See Figure S8 for more details. This absorption is again significant for IR light harvesting. Further the tunable absorption properties of the s-SWCNTs reported here are expected to serve as new design inspirations for saturable absorbers in IR lasers.⁶⁶

CONCLUSIONS

In summary, the gate-tunable complex refractive index of the ultrathin high-purity s-SWCNT films is investigated by SE. We

observe that the complex refractive index of the s-SWCNT films shows a variation of up to 15% in the near-IR region as V_G changes from -50 V to +50 V. This large change can be mainly attributed to the intense PDE and exciton effect. We further find that the s-SWCNT films shows the highest sensitivity to change in optical constants (Δn and $\Delta \alpha$) as a function the externally applied electric fields, at the telecom wavelengths of 1.3 and 1.55 um in comparison to all bulk and conventional EO semiconductors and insulators. Finally, a multilayer superlattice stack-based IR reflection phase modulator based on s-SWCNT and 1L-MoS₂ is designed, which achieves a >45° EO reflection phase modulation in the near IR. Our results suggest that highpurity s-SWCNTs are very promising as highly tunable EO materials particularly in the telecommunications range. Given the magnitude of index modulation observed, our results should promote the development of SWCNT-based IR tunable optoelectronics devices, such as modulators, limiters, and saturable absorbers.

METHODS

Preparation of s-SWCNT. The ultrathin s-SWCNT films are deposited onto a 4 in. SiO_2/Si by dip-coating using a chloroform-dispersed high-purity (>99%) semiconducting SWCNT dispersion detailed in our prior publications. ^{23,24}

Characterization of s-SWCNT. The typical Raman spectrum of s-SWCNT films was measured by an integrated confocal spectrum testing and analysis system. The scattered Raman signals were collected by a microscope objective (Olympus SLMPLN 100×) and analyzed using a grating spectrometer coupled to a Si focal plane array (FPA) detector. All these instruments are integrated into the LabRAM HR Evolution confocal microscope. The wavelength of the excitation laser is 633 nm (1.96 eV) and the lateral size of the measurement spot is less than 1 μ m. The spectroscopic ellipsometer used in our experiment is M-2000 type spectroscopic ellipsometer purchased from J. A. Woollam Company, whose detector spectral range is 371-1687 nm (0.73-3.34 eV). The multi-incidence measurement mode (angle of incidence (AOI): 60°, 65°, and 70°) was adopted to measure the s-SWCNT films.

ASSOCIATED CONTENT

Supporting Information

The Supporting Information is available free of charge at https://pubs.acs.org/doi/10.1021/acsphotonics.0c01220.

Raman analysis of s-SWCNT film; Spectroscopic Ellipsometry of s-SWCNT specimen; Complex refractive indices of Arc discharge and HiPco s-SWCNT films; Gate-tunable ellipsometry spectra of s-SWCNT film; Optimization results of (1L-MoS₂/SWCNT)₅/MoS₂/Au near-IR gate-tunable reflection phase modulator; Optimization results of (1L-MoS₂/SWCNT)₅/MoS₂/Au near-IR absorber; Tabulated Δn and $\Delta \kappa$ of s-SWCNT, some traditional semiconductors, and QW structures (PDF)

AUTHOR INFORMATION

Corresponding Authors

Shiyuan Liu — School of Mechanical Science and Engineering, Huazhong University of Science and Technology, Wuhan 430074, People's Republic of China; ⊚ orcid.org/0000-0002-0756-1439; Email: shyliu@hust.edu.cn

Deep Jariwala — Department of Electrical and Systems Engineering, University of Pennsylvania, Philadelphia, Pennsylvania 19104, United States; ⊚ orcid.org/0000-0002-3570-8768; Email: dmj@seas.upenn.edu

Authors

- Baokun Song Department of Electrical and Systems
 Engineering, University of Pennsylvania, Philadelphia,
 Pennsylvania 19104, United States; School of Mechanical Science
 and Engineering, Huazhong University of Science and
 Technology, Wuhan 430074, People's Republic of China
- Fang Liu Center for Carbon-Based Electronics and Key Laboratory for the Physics and Chemistry of Nanodevices, Department of Electronics, Peking University, Beijing 100871, People's Republic of China
- Haonan Wang Department of Chemistry, University of Pennsylvania, Philadelphia, Pennsylvania 19104, United States; orcid.org/0000-0003-2047-5380
- Jinshui Miao Department of Electrical and Systems Engineering, University of Pennsylvania, Philadelphia, Pennsylvania 19104, United States
- Yueli Chen Department of Chemistry, University of Pennsylvania, Philadelphia, Pennsylvania 19104, United States
- Pawan Kumar Department of Electrical and Systems
 Engineering and Department of Materials Science and
 Engineering, University of Pennsylvania, Philadelphia,
 Pennsylvania 19104, United States; orcid.org/0000-0002-5764-2915
- Huiqin Zhang Department of Electrical and Systems Engineering, University of Pennsylvania, Philadelphia, Pennsylvania 19104, United States
- Xiwen Liu Department of Electrical and Systems Engineering, University of Pennsylvania, Philadelphia, Pennsylvania 19104, United States
- Honggang Gu School of Mechanical Science and Engineering, Huazhong University of Science and Technology, Wuhan 430074, People's Republic of China; ○ orcid.org/0000-0001-8812-1621
- Eric A. Stach Department of Materials Science and Engineering, University of Pennsylvania, Philadelphia, Pennsylvania 19104, United States; Oorcid.org/0000-0002-3366-2153
- Xuelei Liang Center for Carbon-Based Electronics and Key Laboratory for the Physics and Chemistry of Nanodevices, Department of Electronics, Peking University, Beijing 100871, People's Republic of China
- Zahra Fakhraai Department of Chemistry, University of Pennsylvania, Philadelphia, Pennsylvania 19104, United States; orcid.org/0000-0002-0597-9882

Complete contact information is available at: https://pubs.acs.org/10.1021/acsphotonics.0c01220

Notes

The authors declare no competing financial interest.

ACKNOWLEDGMENTS

D.J. acknowledges primary support for this work by the U.S. Army Research Office under Contract Number W911NF-19-1-0109. D.J. and E.A.S. also acknowledge support from National Science Foundation (DMR-1905853). D.J., E.A.S., and Z.F. acknowledge partial support from University of Pennsylvania Materials Research Science and Engineering Center (MRSEC; DMR-1720530). H.Z. acknowledges support from the Vagelos Institute of Energy Science and Technology graduate fellowship.

B.S. acknowledges the support from China scholarship council (CSC). B.S., H.G., and S.L. acknowledge the National Natural Science Foundation of China (51525502 and 51775217). X.L. and F.L. acknowledge support from National Key Research and Development Program (No. 2016YFA0201902) and the National Natural Science Foundation of Chine (No. 61621061). A portion of this work was carried out at the Singh Center for Nanotechnology at the University of Pennsylvania, which is supported by the National Science Foundation (NSF) National Nanotechnology Coordinated Infrastructure Program Grant NNCI-1542153.

REFERENCES

- (1) Reed, G. T.; Mashanovich, G.; Gardes, F. Y.; Thomson, D. J. Silicon optical modulators. *Nat. Photonics* **2010**, *4*, 518–526.
- (2) Chen, A.; Murphy, E. J. Broadband Optical Modulators: Science, Technology, and Applications; CRC Press: Boca Raton, FL, 2012; pp 129–203.
- (3) Sun, Z.; Martinez, A.; Wang, F. Optical modulators with 2D layered materials. *Nat. Photonics* **2016**, *10*, 227–238.
- (4) Wakita, K. Semiconductor Optical Modulators; Kluwer Academic Publishers: Boston, 1998; pp 41–111.
- (5) Pavesi, L., Lockwood, D. J., Eds. In Silicon Photonics; Springer, 2004; pp 1–250.
- (6) Liu, A.; Liao, L.; Rubin, D.; Nguyen, H.; Ciftcioglu, B.; Chetrit, Y.; Izhaky, N.; Paniccia, M. High-speed optical modulation based on carrier depletion in a silicon waveguide. *Opt. Express* **2007**, *15*, 660–668
- (7) Soref, R. A.; Bennett, B. R. Electrooptical effects in silicon. *IEEE J. Ouantum Electron.* **1987**, 23, 123–129.
- (8) Jalili, Y. S.; Stavrinou, P. N.; Roberts, J. S.; Parry, G. Electroabsorption and electro-refraction in InGaAsN quantum well structures. *Electron. Lett.* **2002**, *38*, 343–344.
- (9) Kuo, Y. H.; Lee, Y. K.; Ge, Y.; Ren, S.; Roth, J. E.; Kamins, T. I.; Miller, D. A. B.; Harris, J. S. Strong quantum-confined Stark effect in germanium quantum-well structures on silicon. *Nature* **2005**, *437*, 1334–1336.
- (10) Zhang, Q.; Zhen, Z.; Yang, Y.; Gan, G.; Jariwala, D.; Cui, X. Hybrid phonon-polaritons at atomically-thin van der Waals heterointerfaces for infrared optical modulation. *Opt. Express* **2019**, 27, 18585–18600.
- (11) Liu, Y.; Willis, R. F. Plasmon-phonon strongly coupled mode in epitaxial graphene. *Phys. Rev. B: Condens. Matter Mater. Phys.* **2010**, *81*, 081406
- (12) Brar, V. W.; Jang, M. S.; Sherrott, M.; Kim, S.; Lopez, J. J.; Kim, L. B.; Choi, M.; Atwater, H. Hybrid surface-phonon-plasmon polariton modes in graphene/monolayer h-BN heterostructures. *Nano Lett.* **2014**, *14*, 3876–3880.
- (13) Dai, S.; Fei, Z.; Ma, Q.; Rodin, A. S.; Wagner, M.; McLeod, A. S.; Liu, M. K.; Gannett, W.; Regan, W.; Watanabe, K.; Taniguchi, T.; Thiemens, M.; Dominguez, G.; Castro Neto, A. H.; Zettl, A.; Keilmann, F.; Jarillo-Herrero, P.; Fogler, M. M.; Basov, D. N. Tunable phonon polaritons in atomically thin van der Waals crystals of boron nitride. *Science* **2014**, 343, 1125–1129.
- (14) Xia, F.; Wang, H.; Xiao, D.; Dubey, M.; Ramasubramaniam, A. Two-dimensional material nanophotonics. *Nat. Photonics* **2014**, *8*, 899–907.
- (15) Yu, Y.; Yu, Y.; Huang, L.; Peng, H.; Xiong, L.; Cao, L. Giant gating tunability of optical refractive index in transition metal dichalcogenide monolayers. *Nano Lett.* **2017**, *17*, 3613–3618.
- (16) Kravets, V. G.; Wu, F.; Auton, G. H.; Yu, T.; Imaizumi, S.; Grigorenko, A. N. Measurements of electrically tunable refractive index of MoS₂ monolayer and its usage in optical modulators. *npj 2D Mater. Appl.* **2019**, *3*, 36.
- (17) Dresselhaus, M. S.; Dresselhaus, G.; Avouris, P. Carbon Nanotubes: Synthesis, Structure, Properties and Applications; Springer: New York, 2000; pp 57–77.

- (18) Perebeinos, V.; Avouris, P. Exciton ionization, Franz-Keldysh, and Stark effects in carbon nanotubes. *Nano Lett.* **2007**, 7, 609–613.
- (19) Kishida, H.; Nagasawa, Y.; Imamura, S.; Nakamura, A. Direct observation of dark excitons in micelle-wrapped single-wall carbon nanotubes. *Phys. Rev. Lett.* **2008**, *100*, 097401.
- (20) Yoshida, M.; Kumamoto, Y.; Ishii, A.; Yokoyama, A.; Kato, Y. K. Stark effect of excitons in individual air-suspended carbon nanotubes. *Appl. Phys. Lett.* **2014**, *105*, 161104.
- (21) Wu, Z.; Chen, Z.; Du, X.; Logan, J. M.; Sippel, J.; Nikolou, M.; Kamaras, K.; Reynolds, J. R.; Tanner, D. B.; Hebard, A. F.; Rinzler, A. G. Transparent, conductive carbon nanotube films. *Science* **2004**, *305*, 1273–1276.
- (22) Takenobu, T.; Murayama, Y.; Iwasa, Y. Optical evidence of Stark effect in single-walled carbon nanotube transistors. *Appl. Phys. Lett.* **2006**, *89*, 263510.
- (23) Dong, G.; Zhao, J.; Shen, L.; Xia, J.; Meng, H.; Yu, W.; Huang, Q.; Han, H.; Liang, X.; Peng, L.-M. Large-area and highly uniform carbon nanotube film for high-performance thin film transistors. *Nano Res.* **2018**, *11*, 4356–4367.
- (24) Xia, J.; Dong, G.; Tian, B.; Yan, Q.; Zhang, H.; Liang, X.; Peng, L.-M. Metal contact effect on the performance and scaling behavior of carbon nanotube thin film transistors. *Nanoscale* **2016**, *8*, 9988–9996.
- (25) Liu, L.; Han, J.; Xu, L.; Zhou, J.; Zhao, C.; Ding, S.; Shi, H.; Xiao, M.; Ding, L.; Ma, Z.; Jin, C.; Zhang, Z.; Peng, L.-M. Aligned, high-density semiconducting carbon nanotube arrays for high-performance electronics. *Science* **2020**, *368*, 850–856.
- (26) Geier, M. L.; Prabhumirashi, P. L.; McMorrow, J. J.; Xu, W.; Seo, J.-W. T.; Everaerts, K.; Kim, C. H.; Marks, T. J.; Hersam, M. C. Subnanowatt carbon nanotube complementary logic enabled by threshold voltage control. *Nano Lett.* **2013**, *13*, 4810–4814.
- (27) Geier, M. L.; McMorrow, J. J.; Xu, W.; Zhu, J.; Kim, C. H.; Marks, T. J.; Hersam, M. C. Solution-processed carbon nanotube thin-film complementary static random access memory. *Nat. Nanotechnol.* **2015**, *10*, 944–948.
- (28) Liu, H.; Nishide, D.; Tanaka, T.; Kataura, H. Large-scale single-chirality separation of single-wall carbon nanotubes by simple gel chromatography. *Nat. Commun.* **2011**, *2*, 1–8.
- (29) Kataura, H.; Kumazawa, Y.; Maniwa, Y.; Umezu, I.; Suzuki, S.; Ohtsuka, Y.; Achiba, Y. Optical properties of single-wall carbon nanotubes. *Synth. Met.* **1999**, *103*, 2555–2558.
- (30) Shulaker, M. M.; Hills, G.; Patil, N.; Wei, H.; Chen, H.-Y.; Wong, H.-S. P.; Mitra, S. Carbon nanotube computer. *Nature* **2013**, *501*, *526*–530
- (31) Shulaker, M. M.; Hills, G.; Park, R. S.; Howe, R. T.; Saraswat, K.; Wong, H.-S. P.; Mitra, S. Three-dimensional integration of nanotechnologies for computing and data storage on a single chip. *Nature* **2017**, *547*, 74–78.
- (32) Simpson, J. R.; Roslyak, O.; Duque, J. G.; Hároz, E. H.; Crochet, J. J.; Telg, H.; Piryatinski, A.; Walker, A. R. H.; Doorn, S. K. Resonance Raman signature of intertube excitons in compositionally-defined carbon nanotube bundles. *Nat. Commun.* **2018**, *9*, 637.
- (33) Dresselhaus, M. S.; Dresselhaus, G.; Saito, R.; Jorio, A. Raman spectroscopy of carbon nanotubes. *Phys. Rep.* **2005**, *409*, 47–99.
- (34) Jorio, A.; Dresselhaus, G.; Dresselhaus, M. S.; Souza, M.; Dantas, M. S. S.; Pimenta, M. A.; Rao, A. M.; Saito, R.; Liu, C.; Cheng, H. M. Polarized Raman study of single-wall semiconducting carbon nanotubes. *Phys. Rev. Lett.* **2000**, *85*, 2617–2620.
- (35) Zhang, D.; Yang, J.; Yang, F.; Li, R.; Li, M.; Ji, D.; Li, Y. (*n*,*m*) Assignments and quantification for single-walled carbon nanotubes on SiO₂/Si substrates by resonant Raman spectroscopy. *Nanoscale* **2015**, *7*, 10719–10727.
- (36) Miyata, Y.; Yanagi, K.; Maniwa, Y.; Kataura, H. Optical properties of metallic and semiconducting single-wall carbon nanotubes. *Phys. Status Solidi B* **2008**, 245, 2233–2238.
- (37) Ding, J.; Li, Z.; Lefebvre, J.; Cheng, F.; Dubey, G.; Zou, S.; Finnie, P.; Hrdina, A.; Scoles, L.; Lopinski, G. P.; Kingston, C. T.; Simard, B.; Malenfant, P. R. L. Enrichment of large-diameter semiconducting SWCNTs by polyfluorene extraction for high network density thin film transistors. *Nanoscale* **2014**, *6*, 2328–2339.

- (38) Pettersson, L. A. A.; Roman, L. S.; Inganäs, O. Modeling photocurrent action spectra of photovoltaic devices based on organic thin films. *J. Appl. Phys.* **1999**, *86*, 487–496.
- (39) Fujiwara, H. Spectroscopic Ellipsometry: Principles and Applications; John Wiley & Sons: Chichester, 2007; pp 81–207.
- (40) Leguy, A. M. A.; Azarhoosh, P.; Alonso, M. I.; Campoy-Quiles, M.; Weber, O. J.; Yao, J.; Bryant, D.; Weller, M. T.; Nelson, J.; Walsh, A.; van Schilfgaarde, M.; Barnes, P. R. F. Experimental and theoretical optical properties of methylammonium lead halide perovskites. *Nanoscale* **2016**, *8*, 6317–6327.
- (41) Song, B.; Gu, H.; Fang, M.; Chen, X.; Jiang, H.; Wang, R.; Zhai, T.; Ho, Y.-T.; Liu, S. Layer-dependent dielectric function of wafer-scale 2D MoS₂. *Adv. Opt. Mater.* **2019**, *7*, 1801250.
- (42) Song, B.; Gu, H.; Fang, M.; Ho, Y.-T.; Chen, X.; Jiang, H.; Liu, S. Complex optical conductivity of two-dimensional MoS₂: A striking layer dependency. *J. Phys. Chem. Lett.* **2019**, *10*, 6246–6252.
- (43) Nelson, F. J.; Kamineni, V. K.; Zhang, T.; Comfort, E. S.; Lee, J. U.; Diebold, A. C. Optical properties of large-area polycrystalline chemical vapor deposited graphene by spectroscopic ellipsometry. *Appl. Phys. Lett.* **2010**, *97*, 253110.
- (44) Jariwala, D.; Sangwan, V. K.; Wu, C.-C.; Prabhumirashi, P. L.; Geier, M. L.; Marks, T. J.; Lauhon, L. J.; Hersam, M. C. Gate-tunable carbon nanotube-MoS₂ heterojunction pn diode. *Proc. Natl. Acad. Sci. U. S. A.* **2013**, *110*, 18076–18080.
- (45) Sherrott, M. C.; Whitney, W. S.; Jariwala, D.; Biswas, S.; Went, C. M.; Wong, J.; Rossman, G. R.; Atwater, H. A. Anisotropic quantum well electro-optics in few-layer black phosphorus. *Nano Lett.* **2019**, *19*, 269–276
- (46) Liu, K.; Deslippe, J.; Xiao, F.; Capaz, R. B.; Hong, X.; Aloni, S.; Zettl, A.; Wang, W.; Bai, X.; Louie, S. G.; Wang, E.; Wang, F. An atlas of carbon nanotube optical transitions. *Nat. Nanotechnol.* **2012**, *7*, 325–329.
- (47) Kane, C. L.; Mele, E. J. Electron interactions and scaling relations for optical excitations in carbon nanotubes. *Phys. Rev. Lett.* **2004**, 93, 197402.
- (48) Simien, D.; Fagan, J. A.; Luo, W.; Douglas, J. F.; Migler, K.; Obrzut, J. Influence of Nanotube length on the optical and conductivity properties of thin single-wall carbon nanotube networks. *ACS Nano* **2008**, *2*, 1879–1884.
- (49) Van Eck, T. E.; Walpita, L. M.; Chang, W. S. C.; Wieder, H. H. Franz-Keldysh electrorefraction and electroabsorption in bulk InP and GaAs. *Appl. Phys. Lett.* **1986**, *48*, 451–453.
- (50) Gray, P. R.; Hurst, P.; Lewis, S. H.; Meyer, R. G. Analysis and Design of Analog Integrated Circuits; Wiley, 2001; pp 1-73.
- (51) Jakubka, F.; Grimm, S. B.; Zakharko, Y.; Gannott, F.; Zaumseil, J. Trion electroluminescence from semiconducting carbon nanotubes. *ACS Nano* **2014**, *8*, 8477–8486.
- (52) Wendland, P. H.; Chester, M. Electric field effects on indirect optical transitions in silicon. *Phys. Rev.* **1965**, *140*, 1384–1390.
- (53) Seraphin, B. O.; Bottka, N. Franz-Keldysh effect of the refractive index in semiconductors. *Phys. Rev.* **1965**, *139*, 560–565.
- (54) Frigerio, J.; Vakarin, V.; Chaisakul, P.; Ferretto, M.; Chrastina, D.; Le Roux, X.; Vivien, L.; Isella, G.; Marris-Morini, D. Giant electro-optic effect in GeSiGe coupled quantum wells. *Sci. Rep.* **2015**, *5*, 1–8.
- (55) Nagarajan, R; Kato, M; Pleumeekers, J; Evans, P; Corzine, S; Hurtt, S; Dentai, A; Murthy, S; Missey, M; Muthiah, R; Salvatore, R A; Joyner, C; Schneider, R.; Ziari, M; Kish, F; Welch, D InP photonic integrated circuits. *IEEE J. Sel. Top. Quantum Electron.* **2010**, *16*, 1113–1125.
- (56) Wang, C.; Zhang, M.; Chen, X.; Bertrand, M.; Shams-Ansari, A.; Chandrasekhar, S.; Winzer, P.; Lončar, M. Integrated lithium niobate electro-optic modulators operating at CMOS-compatible voltages. *Nature* **2018**, *562*, 101–104.
- (57) Palik, E. D. *Handbook of Optical Constants of Solids*; Academic: New York, 1998; Vol. *I*, pp 699–700.
- (58) Arizmendi, L. Photonic applications of lithium niobate crystals. *Phys. Stat. Sol.* (a) **2004**, 201, 253–283.
- (59) Volodin, B. L. Highly efficient photorefractive polymers for dynamic holography. *Opt. Eng.* **1995**, 34, 2213–2223.

- (60) Li, Z. Q.; Henriksen, E. A.; Jiang, Z.; Hao, Z.; Martin, M. C.; Kim, P.; Stormer, H. L.; Basov, D. N. Dirac charge dynamics in graphene by infrared spectroscopy. *Nat. Phys.* **2008**, *4*, 532–535.
- (61) Avouris, P.; Freitag, M.; Perebeinos, V. Carbon-nanotube photonics and optoelectronics. *Nat. Photonics* **2008**, *2*, 341–350.
- (62) Beal, A. R.; Hughes, H. P. Kramers-Kronig analysis of the reflectivity spectra of 2H-MoS₂, 2H-MoSe₂ and 2H-MoTe₂. *J. Phys. C: Solid State Phys.* **1979**, 12, 881–890.
- (63) Born, M.; Wolf, E. Principles of Optics: Electromagnetic Theory of Propagation, Interference and Diffraction of Light; Elsevier, 2013; pp 286-411.
- (64) Jeong, H. Y.; Kim, U. J.; Kim, H.; Han, G. H.; Lee, H.; Kim, M. S.; Jin, Y.; Ly, T. H.; Lee, S. Y.; Roh, Y.-G.; Joo, W.-J.; Hwang, S. W.; Park, Y.; Lee, Y. H. Optical gain in MoS₂ via coupling with nanostructured substrate: Fabry–Perot interference and plasmonic excitation. *ACS Nano* **2016**, *10*, 8192–8198.
- (65) Slagmolen, B. J. J.; Gray, M. B.; Baigent, K. G.; McClelland, D. E. Phase-sensitive reflection technique for characterization of a Fabry–Perot interferometer. *Appl. Opt.* **2000**, *39*, 3638–3643.
- (66) Schmidt, A.; Rivier, S.; Steinmeyer, G.; Yim, J. H.; Cho, W. B.; Lee, S.; Rotermund, F.; Pujol, M. C.; Mateos, X.; Aguiló, M.; Díaz, F.; Petrov, V.; Griebner, U. Passive mode locking of Yb: KLuW using a single-walled carbon nanotube saturable absorber. *Opt. Lett.* **2008**, *33*, 729–731.